Journal of Magnetic Resonance 294 (2018) 153–161

Contents lists available at ScienceDirect

Journal of Magnetic Resonance

journal homepage: www.elsevier.com/locate/jmr

Constant gradient elastography with optimal control RF pulses

Eric Van Reeth [a,1,*], Pauline M. Lefebvre [a,1], Hélène Ratiney [a], Simon A. Lambert [a], Michael Tesch [b], Elisabeth Brusseau [a], Denis Grenier [a], Olivier Beuf [a], Steffen J. Glaser [b], Dominique Sugny [c,d], Kevin Tse-Ve-Koon [a]

[a] CREATIS, CNRS UMR5220, INSERM U1206, Université Lyon 1, INSA Lyon, Université Jean Monnet Saint-Etienne, France
[b] Department of Chemistry, Technische Universität München, Germany
[c] ICB, CNRS UMR6303, Université de Bourgogne, France
[d] Institute for Advanced Study, Technische Universität München, Lichtenbergstrasse 2a, D-85748 Garching, Germany

ARTICLE INFO

Article history:
Received 24 May 2018
Revised 16 July 2018
Accepted 17 July 2018
Available online 19 July 2018

Keywords:
Elastography
Optimal control
Pulse design
Bloch equations

ABSTRACT

This article presents a new motion encoding strategy to perform magnetic resonance elastography (MRE). Instead of using standard motion encoding gradients, a tailored RF pulse is designed to simultaneously perform selective excitation and motion encoding in presence of a constant gradient. The RF pulse is designed with a numerical optimal control algorithm, in order to obtain a magnetization phase distribution that depends on the displacement characteristics inside each voxel. As a consequence, no post-excitation encoding gradients are required. This offers numerous advantages, such as reducing eddy current artifacts, and relaxing the constraint on the gradients maximum switch rate. It also allows to perform MRE with ultra-short TE acquisition schemes, which limits T_2 decay and optimizes signal-to-noise ratio. The pulse design strategy is developed and analytically analyzed to clarify the encoding mechanism. Finally, simulations, phantom and *ex vivo* experiments show that phase-to-noise ratios are improved when compared to standard MRE encoding strategies.

1. Introduction

Magnetic resonance elastography (MRE) has become a standard technique to visualize biological tissue displacements induced by shear wave propagation. Mechanical properties of tissues can be derived from the wave characteristics (wavelength, attenuation). It was initially proposed to encode the tissue displacement in the magnetization phase image by applying appropriate time varying gradients after the radio-frequency (RF) excitation [1]. Considering the simple case of pure sinusoidal excitation with no initial phase and a displacement amplitude A, the accumulated phase of an isochromat during the time τ during which the gradient is applied is given by:

$$\Phi(x) = \gamma \int_0^{\tau} G(t) \times A \sin\left(-2\pi f_e t + \frac{2\pi}{\lambda} x\right) dt \quad (1)$$

with x the direction of the wave propagation, γ the gyromagnetic ratio, $G(t)$ the motion encoding gradient (MEG), λ the wavelength and f_e the mechanical excitation frequency. The resulting phase accumulation thus depends on the motion in the direction along which the gradient is applied.

This gradient-based encoding strategy has been included into a variety of MR sequences including gradient echo, spin echo and echo planar imaging; and applied to a large variety of organs such as liver [2], brain [3], heart [4], in both human and animal studies. Improvements to enhance the phase encoding efficiency have also been proposed. Fractional encoding consists in using only fractions of the motion period to encode the wave propagation: $\tau_g < 1/f_e$, with τ_g the gradient-encoding duration [5]. This improves the phase-to-noise ratio for tissues with short relaxation times, as for example in the healthy human liver ($T_2 \approx 34$ ms at 3T [6]) or in livers of patients suffering from nonalcoholic steatohepatitis ($T_2^{\star} \approx 20$ ms [7]). Multi-frequency approaches have also been proposed to encode a motion containing multiple frequencies in a single acquisition [8].

Optimal control theory has been proposed as an efficient RF pulse design tool in MRI. It consists in determining the control, i.e. the RF pulse, that brings the magnetization in a user-defined target state, taking into consideration the dynamics of the system to be optimized. It has mainly been investigated in the context of robust excitation and refocusing [9–18], parallel transmission [19–23], and contrast optimization [24–31]. The ability of optimal

* Corresponding author.
E-mail address: eric.van-reeth@creatis.insa-lyon.fr (E. Van Reeth).
[1] Both authors contributed equally to this work.

https://doi.org/10.1016/j.jmr.2018.07.013
1090-7807/

control theory to produce extremely efficient pulses that take experimental variations into account makes it a valuable pulse design strategy.

Control of the magnetization phase with optimal RF pulses was investigated in the context of NMR [32,33], and applied to delayed echo sequences in MRI [34]. Recently, the creation of non-trivial phase patterns and preliminary applications on mechanical wave encoding with optimal RF pulses were investigated [35]. A crucial initial consideration was to describe the simultaneous application of a constant gradient applied along z, and the wave propagation as a static field variation:

$$\omega_0^{(i)}(t) = \gamma B_0^{(i)}(t) = \gamma G \times A \sin(-2\pi f_e t + \theta^{(i)}) \tag{2}$$

where $\theta^{(i)} = \frac{2\pi}{\lambda} x^{(i)}$, with $x^{(i)}$ representing a specific position along the wave propagation. Using optimal control theory, tailored RF pulses can be computed in order to introduce a specific dependence between the position along the propagation of a given isochromat, and its magnetization phase at the end of the RF application. As a result, the wave characteristics will be contained in the phase of the acquired MR signal. This offers several potential advantages over standard MRE: (i) no phase accumulation step is required after excitation which allows extremely short echo times (TE) and thus potential SNR improvement especially for low-frequency encoding, and (ii) it relaxes the constraint on having periodic gradient oscillations, thus avoiding fast gradient switches which introduce eddy currents, and which can be a hardware limitation at high frequencies.

This article aims at providing a thorough optimal control framework for the computation of optimal RF pulses for MRE. The control problem formulation is simplified to produce time optimal solutions that provide intuitive insight on the phase encoding mechanism. Sections 2 and 3 introduce the optimal control theory and the numerical implementation for the RF pulse computation. Section 4 presents simulation results that quantify the theoretical encoding improvement compared to the standard gradient-based encoding. Finally, phantom and *ex vivo* acquisitions validate the applicability of the proposed approach on a small-animal 4.7 T MRI system. Superior phase-to-noise values are obtained compared to the standard encoding scheme, emphasizing the advantageous compromise between signal-to-noise ratio and phase encoding offered by the proposed method.

2. Optimal control pulse design

2.1. Pontryagin maximum principle

The Pontryagin Maximum Principle (PMP) [36] provides a theoretical framework to compute the control function that optimizes the evolution of a given dynamic system with respect to a user-defined cost function. In the present case of a Mayer problem [24], it is based on the definition of a pseudo-Hamiltonian $H = \vec{P} \cdot \dot{\vec{M}}$, that must fulfill the maximization condition during the whole control time:

$$H(\vec{M^\star}, \vec{P^\star}, \boldsymbol{U}^\star) = \max_{\boldsymbol{U}\in\Omega} H(\vec{M^\star}, \vec{P^\star}, \boldsymbol{U}) \tag{3}$$

with Ω the set of admissible controls, $\vec{M}$ and $\vec{P}$ respectively the state and costate variables and $\boldsymbol{U} = (u_x, u_y)$, the control field.

Moreover, the optimal state and costate variables fulfill the Hamiltonian equations:

$$\dot{\vec{M}} = \frac{\partial H}{\partial \vec{P}}; \quad \dot{\vec{P}} = -\frac{\partial H}{\partial \vec{M}} \tag{4}$$

with the boundary conditions, which in our case reduce to:

$$\vec{M}(t_0) = \begin{pmatrix} 0 \\ 0 \\ M_0 \end{pmatrix}; \quad \vec{P}(t_f) = -\frac{\partial C}{\partial \vec{M}}(\vec{M}(t_f)) \tag{5}$$

Here, C represents the user-defined cost function and $[t_0, t_f]$ the control time interval.

In the present study, the state variable is the magnetization vector, whose evolution is governed by the Bloch equations:

$$\begin{pmatrix} \dot{M}_x \\ \dot{M}_y \\ \dot{M}_z \end{pmatrix} = \begin{pmatrix} -\frac{1}{T_2} & \omega_0 & -u_y \\ -\omega_0 & -\frac{1}{T_2} & u_x \\ u_y & -u_x & -\frac{1}{T_1} \end{pmatrix} \begin{pmatrix} M_x \\ M_y \\ M_z \end{pmatrix} + \begin{pmatrix} 0 \\ 0 \\ \frac{M_0}{T_1} \end{pmatrix} \tag{6}$$

with ω_0 the resonance offset, M_0 the equilibrium magnetization and (u_x, u_y) respectively the x and y components (in the rotating frame of reference) of the RF pulse to be optimized.

The PMP, as stated here, defines a non-trivial system of coupled equations with fixed boundary conditions at initial time for $\vec{M}$ and final time for $\vec{P}$, that can be solved with various numerical optimization strategies [17,37].

2.2. Numerical resolution

The GRAPE algorithm is a gradient descent based algorithm initially introduced for Nuclear Magnetic Resonance optimal pulse design [37]. It aims at computing the optimal RF pulse and magnetization trajectories that fulfill the aforementioned optimality conditions. Starting from an initial guess, the control field is iteratively updated to improve the cost function at each step, while fulfilling the constraints imposed by the PMP. The gradient calculation is based on the forward propagation of the magnetization, and the backward propagation of the costate state as was proposed in the initial implementation [37]. The basic version of the algorithm can be summarized in the following steps:

1. Choice of the initial control field $\boldsymbol{U}^{(0)}$
2. Forward propagation of $\vec{M}(t)$ from t_0 to t_f
3. Backward propagation of $\vec{P}(t)$ from t_f to t_0
4. Update of the current control field from the previous estimation:

$$\boldsymbol{U}^{(k+1)} = \boldsymbol{U}^{(k)} - \alpha \frac{\partial C}{\partial \boldsymbol{U}}$$

with $\alpha > 0$, the convergence step.

5. Repeat steps 2 to 4 until convergence is reached.

Note that the convergence scheme can be improved by using a second order approximation via the implementation of a lBFGS method [38]. Convergence is considered reached when the gradient norm or the step norm are below a given threshold, set to 10^{-8} in this study.

2.3. Cost function

A judicious definition of the cost function is essential to ensure that the optimization process fits the problem at stake. A simple choice consists in minimizing the square of the L_2-norm of the difference between the final magnetization states $\vec{M}^{(i)}(t_f)$, and user-defined target states $\vec{T}^{(i)}$:

$$C(\boldsymbol{U}) = \sum_{i=1}^{N} \|\vec{M}^{(i)}(t_f) - \vec{T}^{(i)}\|^2 \tag{7}$$

with N the total number of considered magnetization trajectories. As pointed out in Eq. (2), the temporal evolution of each magnetization vector (i.e. its trajectory $\vec{M}^{(i)}(t)$) results from a specific static field evolution $B_0^{(i)}(t)$. The target states are chosen as:

$$\vec{T}^{(i)} = \rho \begin{pmatrix} \cos(\Phi^{(i)}) \\ \sin(\Phi^{(i)}) \\ 0 \end{pmatrix} \tag{8}$$

with $\Phi^{(i)}$ the targeted magnetization phase, and ρ the magnetization amplitude. The objective is to introduce a specific dependency between the position of the isochromat along the wave propagation, and the magnetization phase: $\left(\theta^{(i)} \rightarrow \Phi^{(i)}\right)$, while maximizing the transverse magnetization norm at the end of excitation ($\rho = 1$). In practice, the optimization problem is tackled using a finite number of phase steps in the interval $\theta \in [0, 2\pi[$. Section 3 presents a simplified optimization example to illustrate that under certain conditions, it is possible to converge towards a pulse that continuously encodes the wave propagation inside the magnetization phase using only $N = 2$ trajectories.

2.4. Slice selectivity

The simultaneous application of a gradient and a RF pulse implicitly imposes that frequency selectivity must be handled. This is taken into account in the optimization problem by considering isochromats located at different positions in the slice ($z^{(j)}$), i.e. at different resonance offsets. As a consequence, Eq. (2) becomes:

$$\omega_0^{(i,j)}(t) = \gamma G\left(A\sin(-\omega_e t + \theta^{(i)}) + z^{(j)}\right) \tag{9}$$

Different target states will thus be attributed whether the considered isochromat is located in the passband (Δz_{in}) or in the stopband (Δz_{out}), as illustrated in Fig. 1. The passband is related to the desired slice thickness inside which the motion must be consistently encoded in the magnetization phase. Isochromats lying in the stopband are attributed a magnetization target state corresponding to the equilibrium state. As a final step, a low-pass filter (typically a Blackman window) is applied to the pulse with a cut-off frequency set to the corresponding maximum value of Δz_{out}. This ensures that the pulse does not significantly affect magnetization trajectories lying beyond Δz_{out}, while preserving the pulse content inside Δz_{in}.

In practice, the passband and the stopband are discretized to perform the numerical optimization. The cost function defined in Eq. (7) becomes:

$$C(\boldsymbol{U}) = \sum_{j=1}^{J}\sum_{i=1}^{N} \|\vec{M}^{(i,j)}(t_f) - \vec{T}^{(i,j)}\|^2 \tag{10}$$

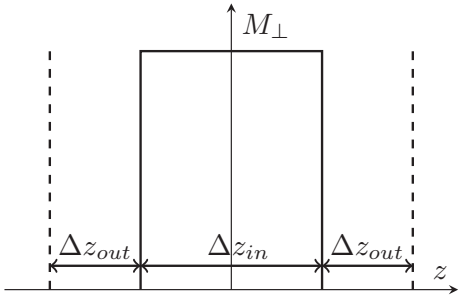

Fig. 1. Ideal slice profile.

with $\vec{T}^{(i,j)} = \rho\left(\cos(\Phi^{(i)}), \sin(\Phi^{(i)}), 0\right)'$ if $j \in \Delta z_{in}$, and $\vec{T}^{(i,j)} = (0, 0, 1)'$ if $j \in \Delta z_{out}$.

In a first step, the pulse is optimized by considering trajectories on resonance only ($J = 1$, i.e. at $z = 0$). The position range J is then iteratively increased until the entire interval is considered. The discretization period is set to 25 Hz, i.e. the optimization process controls magnetization trajectories whose resonance offsets are taken every 25 Hz. This value was chosen as a good compromise between the number of controlled trajectories and the control consistency, i.e. the consistent behavior of the isochromats lying within the 25 Hz interval.

3. Theoretical development

3.1. Framework

Let us consider two isochromats with infinite relaxation times, submitted to the simultaneous application of a periodic mechanical excitation and a constant gradient. They are distant by a quarter of a wavelength, i.e. $\theta^{(1)} = 0$ and $\theta^{(2)} = \pi/2$, situated at the slice center ($z = 0$), i.e. without frequency offsets. Their corresponding magnetization trajectories are: $\vec{M}^{(1)}$ and $\vec{M}^{(2)}$. They are attributed arbitrary magnetization target phases: $\Phi^{(1)} = 0$ and $\Phi^{(2)} = \pi/2$.

The control field is optimized with respect to the previously defined cost function (Eq. (7)). Note that the optimized control field is assumed to have only real values. It will be subsequently verified that this does not restrict the phase encoding performance.

3.2. Results

The optimized pulse and both resulting magnetization trajectories are given in Fig. 2. Interestingly, the solution returned by the numerical optimization process can be intuitively interpreted. An initial $\pi/2$-pulse transfers the magnetization into the transverse plane, followed by π-pulses applied every $\tau_e/2$, with $\tau_e = 1/f_e$. At the end of the pulse, both magnetization trajectories have reached their target states, resulting in a relative phase difference of $\pi/2$ between both isochromats. Isochromat 1 accumulates some phase during the pulse because each π-pulse is synchronized with the sign switches of the static field $B_0^{(1)}$. On the other hand, the phase accumulated by isochromat 2 is null since the π-pulses are applied when $B_0^{(2)}$ reaches its extrema: the phase accumulated during a half-period is canceled during the following half-period.

3.3. Analytical pulse analysis

An analytic description of the phase encoding mechanism can be performed with the following assumptions: (i) both isochromats have the same phase after the application of an ideal $\pi/2$-pulse (without loss of generality, this initial phase is set to 0), (ii) π-pulses are ideal and instantaneously applied every $\tau_e/2$, (iii) infinite relaxation times are considered. In this context, exact solutions of the Bloch equations can be written between each π-pulse:

$$\begin{aligned} \dot{M}_{xy}(t) &= -i\omega_0(t)M_{xy}(t) \\ M_{xy}(t) &= Ke^{-i\frac{\gamma AG}{\omega_e}\cos(-\omega_e t+\theta)} \end{aligned} \tag{11}$$

with $M_{xy}(t) = M_x(t) + iM_y(t)$ the complex magnetization, γ the gyromagnetic ratio, $\omega_0(t)$ representing the static field temporal evolution defined in Eq. (2), and $K \in \mathbb{C}$ a constant term determined with the adequate boundary condition. At $t = \tau_e^-/2$ (before the application of the first π-pulse), this leads to:

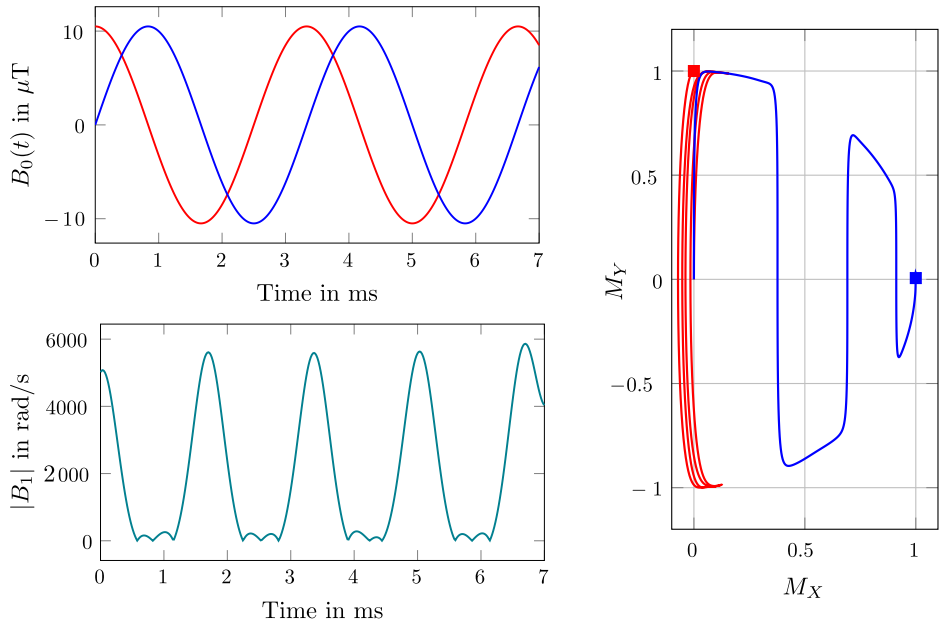

Fig. 2. Illustration of the intuitive RF pulse obtained in the ideal case. Top left: Static field variations perceived by isochromat 1 (blue) and 2 (red). Bottom left: Magnitude of the optimized B_1 pulse. A $\pi/2$-pulse followed by a train of 4 π-pulses applied every $\tau_e/2$ consistently encodes the mechanical wave propagation into the magnetization phase. Right: Corresponding magnetization trajectories during the application of the B_1 pulse. (For interpretation of the references to color in this figure legend, the reader is referred to the web version of this article.)

$$M_{xy}\left(\frac{\tau_e^-}{2}\right) = M_{xy}(0)e^{i\Phi}$$

with $\Phi = \frac{\gamma AG\tau_e}{\pi}\cos\theta, M_{xy}(0)$ the initial magnetization at $t = 0$, and taking into account that $\omega_e = 2\pi/\tau_e$.

The application of a refocusing π-pulse applied along the axis defined by the phase Φ_π can be expressed by adding the following exponential term:

$$M_{xy}^{\pi}\left(\frac{\tau_e^+}{2}\right) = M_{xy}(0)e^{i\Phi}e^{2i(\Phi_\pi-\Phi)}$$

Taking $M_{xy}^{\pi}\left(\frac{\tau_e^+}{2}\right)$ as the initial condition of the free magnetization evolution from $\tau_e^+/2$ to τ_e^-, it is now possible to write Eq. (11) as:

$$M_{xy}(\tau_e^-) = M_{xy}(0)e^{2i(\Phi_\pi-\Phi)}$$

which can be generalized as:

$$M_{xy}\left(\frac{N\tau_e^-}{2}\right) = M_{xy}(0)e^{(-1)^{N-1}iN\Phi}e^{2i(-1)^{N-1}\sum_{n=1}^{N-1}(-1)^n\Phi_\pi^{(n)}} \quad (12)$$

with $N \in \mathbb{N}$, and $\Phi_\pi^{(n)}$ the phase of the n-th π-pulse. The second exponential term only adds a constant phase term to the wave encoding phase term contained in the first exponential. For simplicity, and without affecting the phase encoding performance, it can be chosen to set $\left\{\Phi_\pi^{(n)} = 0, \forall n\right\}$, i.e. applying all π-pulses along the x-axis, which reduces Eq. (12) to:

$$M_{xy}\left(\frac{N\tau_e^-}{2}\right) = M_{xy}(0)e^{(-1)^{N-1}iN\Phi} \quad (13)$$

In terms of implementation, this implies that only the real coefficients of the pulse need to be optimized, which reduces the dimensionality of the optimization problem by 2. This also validates the initial choice of a real pulse in part 3.1.

Finally, it can be shown that these results hold regardless of the position z in the slice, if and only if an even number of π-pulses is applied. The generic phase accumulation, considering the z dependence in the static field variation (Eq. (9)), can be expressed as:

$$M_{xy}\left(\frac{N\tau_e^-}{2}\right) = \begin{cases} M_{xy}(0)e^{-iN\Phi}, & \text{if } N \text{ is even} \\ M_{xy}(0)e^{iN\Phi}e^{-i\frac{\gamma Gz\tau_e}{2}}, & \text{if } N \text{ is odd} \end{cases} \quad (14)$$

This equation points out that when π-pulses are applied every half-period, phase coherence within the slice is preserved only if N is even, i.e. when t is a multiple of τ_e.

3.4. Interpretation

It is quite remarkable to notice that the phase accumulation term of Eq. (13) corresponds to the expression obtained with the standard gradient-based (G-B) approach [1]. In the present case, the π-pulses play the same role as the gradient polarity switches. The proposed encoding mechanism thus shares some similarities with the G-B scheme:

- a mechanical wave attenuation results in a lower accumulated phase value
- the encoding mechanism is independent of the wavelength
- similar images can be used as inputs for post-processing algorithms used for the derivation of the sample's mechanical properties

However, significant differences can be noted between both schemes. The tissue displacement is encoded without oscillating gradients, avoiding eddy current effects usually induced by fast gradient switches, and relaxing the maximum gradient switch rate constraint.

The simultaneous application of the RF pulse and a constant gradient imposes (i) that the optimized pulse has a frequency selective profile, and (ii) that only motion perpendicular to the slice orientation can be encoded.

Both schemes also differ in the way post-excitation T_2 signal loss is handled. The G-B scheme inevitably loses signal during the gradient-based encoding step. On the other hand, as relaxation is incorporated into the magnetization evolution model (see Eq. (6)), the pulse optimization process optimally balances the effect

of excitation, relaxation and phase encoding, and allows signal acquisition at minimal TE. As a consequence, the theoretical $\pi/2, \pi$-pulse train scheme is altered and tailored to fit the specific dynamic evolution of the considered problem. The theoretical phase encoding improvement compared to the standard accumulation scheme is quantified in next section.

4. Results

4.1. Simulation framework

This section quantitatively compares the phase encoding efficiency obtained with the proposed RF-B and the standard G-B schemes. The comparison is performed on wide ranges of parameters that have a significant impact on the encoding process. The considered parameters are:

- T_2 values ranging from 10 to 100 ms, which impacts the signal decay before acquisition and thus the SNR.
- the excitation frequency f_e, which varies from 50 to 800 Hz. The higher the frequency, the shorter the encoding time for a given number of encoding periods.
- the static field variation amplitude, i.e. the product: $P = A \times G$.

The comparison metric is given as a ratio $R(\Phi) = \frac{S_{RF}}{S_{GB}}(\Phi)$, where S_{RF} and S_{GB} respectively represent the transverse magnetization norm for the proposed RF-based and the standard gradient-based encoding schemes, at the time when a given phase term Φ is reached between two isochromats situated at different phase steps: $\theta^{(1)}$ and $\theta^{(2)} = \theta^{(1)} + \pi/2$. In other words, $(R(\Phi) > 1)$ signifies that the RF-B method leads to higher SNR than the G-B method for a similar amount of encoded phase. S_{RF} is the transverse magnetization norm of $\vec{M}^{(1)}(t_f)$, when convergence is reached:

$$S_{RF} = \sqrt{\left(M_x^{(1)}\right)^2 + \left(M_y^{(1)}\right)^2}$$

The corresponding phase accumulation term Φ_t is derived, and S_{GB} is computed as:

$$S_{GB} = e^{-t_\Phi/T_2} \quad \text{with} \quad t_\Phi = \frac{\Phi_t \pi}{2\gamma A G}$$

where t_Φ represents the duration required to encode, with oscillating gradients, the same amount of phase Φ_t. It quantifies the post-excitation T_2 decay that occurs during the gradient encoding process. Note that T_2 is considered, and not $T_2^\star$, which means that the presented results hold for refocused excitation schemes only. It is also considered that the effect of T_1 is negligible, and that π-pulses and gradient switches are both ideal and instantaneous.

A plot that illustrates the distribution of the gain ratio R, for various values of T_2, and f_e and a fixed product $P = 0.8\,\mu T$ is given in Fig. 3. It is clear that the impact of the proposed scheme is higher for short T_2 values and low excitation frequencies. The gain ratio steadies for excitation frequencies above 200 Hz, keeping a value of around 1.2 for short T_2. On the other hand, R asymptotically goes to 1 as T_2 increases. This illustrates the ability of the RF-B scheme to efficiently intricate excitation, relaxation and phase encoding when quick signal loss occurs and when long encoding periods are required. An example of a RF pulse optimized for $T_2 = 10$ ms and $f_e = 400$ Hz is given in Fig. 4a. The magnetization trajectories of two isochromats, having both a T_2 of 10 ms, and a phase difference of $\pi/2$ along the wave propagation are illustrated in Fig. 4b. As a comparison, Fig. 4c illustrates the magnetization trajectories of the same isochromats, obtained with a pulse that does not account for T_2 relaxation, i.e. the ideal $\pi/2$-$N\pi$ pulses scheme presented in the previous section. Comparing the final magnetization states in Fig. 4b and c shows that taking the relaxation into account leads to lower phase accumulation but significantly higher signal. This validates the ability of optimal pulses to efficiently balance the phase accumulation and the signal level.

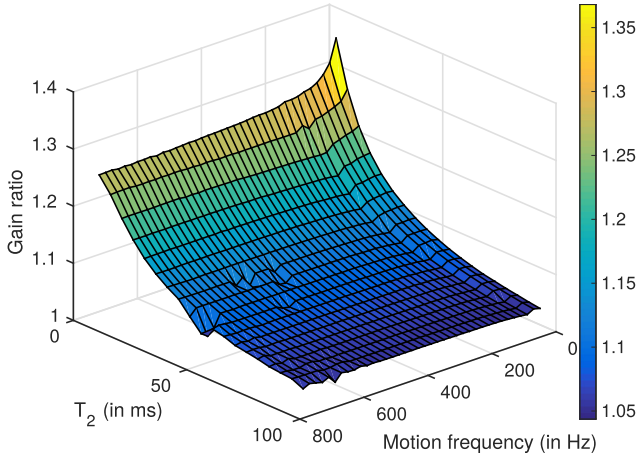

Fig. 3. Distribution of the gain ratio R, for various values of T_2, f_e and a fixed product $P = 0.8\,\mu T$.

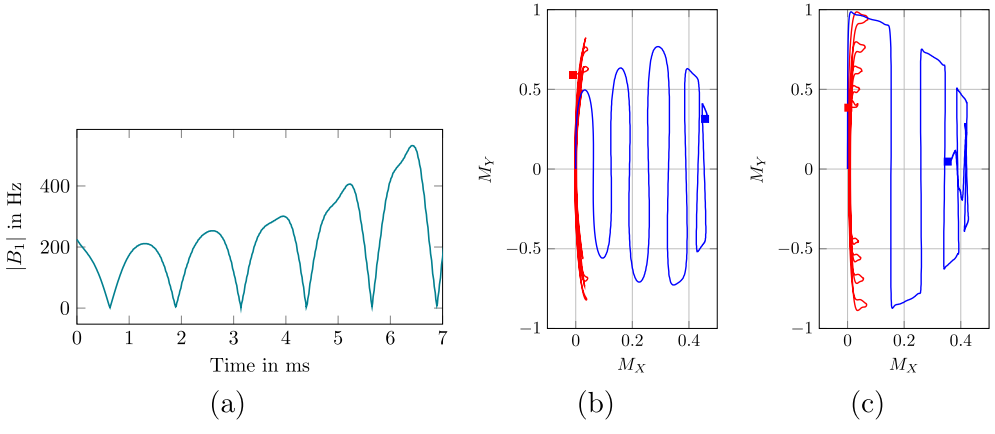

Fig. 4. (a) RF pulse amplitude optimized for T_2 = 10 ms and f_e = 400 Hz (b) Magnetization trajectories of both isochromats having a T_2 of 10 ms, resulting from the application of the RF pulse optimized for T_2 = 10 ms (c) Magnetization trajectories of both isochromats having a T_2 of 10 ms, resulting from the application of the ideal RF that does not account for T_2 relaxation. The squares highlight the final magnetization states.

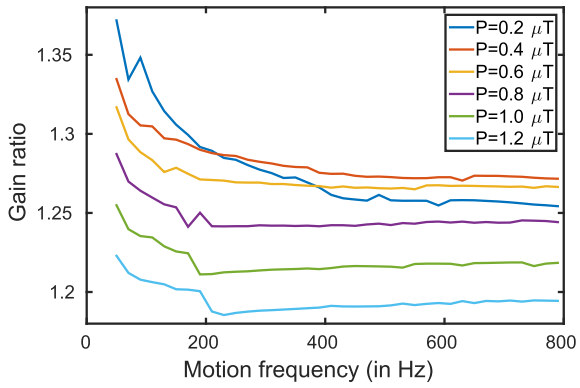

Fig. 5. Gain ratio evolution with respect to various values of $P = A \times G$, for a T_2 value fixed at 15 ms.

As a last parameter, the effect of P is studied. Fig. 5 shows the distribution of R for various values of P, with respect to the excitation frequency for a fixed value of T_2 = 15 ms. As could be expected the gain ratio decreases when P increases: for large values of P, fewer encoding cycles are required to accumulate a given amount of phase, which limits the signal loss after excitation. This also indicates that the RF-B scheme is advantageous in the presence of low motion amplitudes and on MR systems with limited gradient amplitudes. This could also benefit applications where strong attenuation of the wave occurs during the propagation. Next sections present phantom and *ex vivo* experiments in order to evaluate if such results can be confirmed on a practical MR acquisition.

4.2. MRE experiments

4.2.1. Experimental set-up

All experiments were performed on the same Bruker 4.7 T MRI system, with a 70 mm inner diameter volume coil. Shear waves were generated using a custom-made device maintaining the medium between two plates [39]. The upper plate is fixed while the lower one is activated by a piezoelectric actuator (CEDRAT Technologies). A standard plastisol phantom was prepared (Plastileurre Standard, Bricoleurre, France) for the experiment. *Ex vivo* experiments were performed on two different rectangular slabs of the same veal liver. *Ex vivo* tissues were used to determine if observations similar to those from the phantom can still be made with more complex media. To fit at best into the mechanical excitation system which is adapted to media with parallel surfaces, liver tissues needed to be cut accordingly. Two liver pieces are used in order to test the reproducibility of the results on different samples. Although their relaxation times are considered equal, it is likely that their mechanical properties and positioning on the mechanical excitation set-up will vary, which will induce differences in the wave propagation characteristics. T_1 and T_2 values were estimated with a mono-exponential fit of the water signal recovery and decay respectively, using a localized PRESS sequence acquired at various TR and TE. The corresponding values are $[T_1, T_2]$ = [300, 25] ms for the plastisol phantom, and [650, 23] ms for the liver samples. In all acquisitions, the excitation frequency was set to $f_e = 400$ Hz, and the motion encoding gradient was set to $G = 0.15$ T/m. Four different phase offsets (equidistant over one cycle) have been acquired, giving four different snapshots of the wave propagation through each medium. The MR sequence was a turbo spin-echo sequence with an acceleration factor of 2, TR = 1500 ms, FOV = 3.5×3.5 cm^2, NA = 1. The matrix size was set respectively to (64×64) and (128×128) for the *ex vivo* and the phantom experiments. A standard turbo spin-echo MRE sequence (G-B) was implemented, using an equal number of sinusoidal gradient periods before and after the refocusing π-pulse. A maximum of 8 encoding periods was used, since greater values yielded images with impractical SNR values.

The objective of this study is to compare the phase encoding efficiency of the proposed RF-B scheme versus the standard G-B scheme for various numbers of encoding gradient periods (N_G). The comparison metric is defined as the product between the SNR and the maximum phase variation amplitude Δ, in order to quantify the phase-to-noise ratio (PNR):

$$\mathrm{PNR} = \mathrm{SNR} \times \Delta \tag{15}$$

The SNR is computed as the ratio between the average magnitude of a region included in the phantom (R_1 in Fig. 6a), and the standard deviation of a region containing background noise (R_2 in Fig. 6a). The maximum phase variation amplitude is obtained from the phase image, by computing the amplitude (Δ) of a line going through the wave propagation pattern (R_3 in Fig. 6b). A line profile is illustrated in Fig. 6c. If necessary, a one-dimensional unwrapping is performed on the extracted line to compute the exact amplitude variation, as for example in Fig. 6c. Note that all PNR computations are performed at the same phase offset of the wave propagation, on similar regions of interest, and using as many similar sequence parameters as possible.

4.2.2. Optimal Pulse generation

The RF pulse was optimized for an excitation frequency of 400 Hz, a T_2 value of 20 ms, and a duration of 13.8 ms, which corresponds to 5.5 motion periods. A decimal number of period is used in order to allocate some time for the initial $\pi/2$-pulse. The pulse amplitude was bounded during the optimization at 2 kHz (47 μT) in order to fit the RF amplifier power requirements. Slice selectivity parameters (Δz_{in}, Δz_{out}) are set in terms of bandwidth, with respect to the chosen gradient value. The slice bandwidth

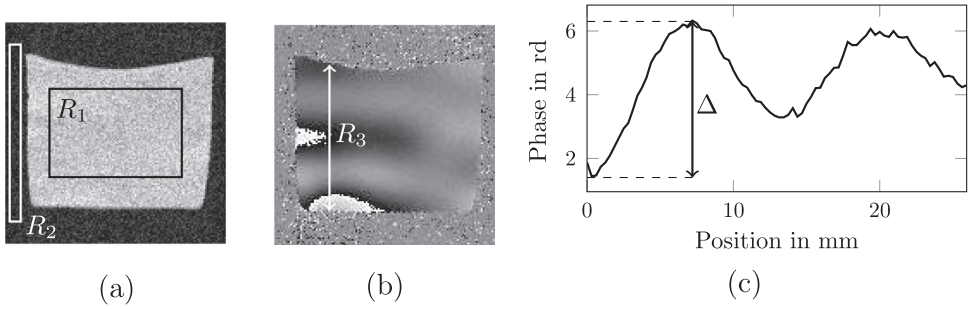

Fig. 6. Phantom results obtained with the RF-B scheme. (a) Magnitude image of the plastisol phantom. R_1 and R_2 respectively represent the signal and noise regions used for the SNR computation. (b) Corresponding raw phase image showing the motion encoding. R_3 represents the line along which the maximum phase variation Δ is computed. (c) Line profile of R_3 after one-dimensional unwrapping.

Δf_{in} interval is set to $[-3, 3]$ kHz (corresponding to $\Delta z_{in} = 0.93$ mm), and the outer bandwidth interval is set to $\pm[4, 13]$ kHz. The final low-pass filtering is performed with a Blackman window with a full width at a half maximum set to 10 kHz. The total duration of the optimization process is around 50 h on a 8-core, 3.1 GHz personal laptop.

The pulse magnitude is displayed in Fig. 7a. A simulated slice profile can be computed by integrating the transverse magnetization inside voxels aligned in the slice selective gradient direction. The simulated slice profile is illustrated in Fig. 7b. The slice profile of the *ex vivo* experiment (liver 1) is presented in Fig. 7c. This image is obtained by acquiring a plane orthogonal to the excited slice. The row by row signal integration of this image provides an average slice profile shown in Fig. 7d, which can be compared with the simulated profile of Fig. 7b. A reasonable match is observed, demonstrating correct in-slice homogeneity and selectivity for the selected resolution parameters. It can be noticed however that the acquired profile is slightly thinner than the simulated profile.

4.2.3. PNR Comparison

The comparison of the phantom and *ex vivo* experiments are presented in Fig. 8. It compares the phase variation amplitude (Δ), the SNR and the resulting PNR obtained with the RF-B scheme and the G-B scheme for different values of N_G. Note that the plotted results are normalized to facilitate the comparison between experiments. As an illustration, the normalized SNR (noted $\overline{SNR}$), of a specific experiment denoted by the index i is computed as:

$$\overline{SNR^i} = \frac{SNR^i}{\max(SNR^j)}$$

for $j = 1, \ldots, N_e$ the index running through all N_e experiments.

As could be expected for the G-B acquisitions, Δ increases with N_G since a longer duration is used for motion encoding. Note, however, that $N_G = 6$ results in higher values of Δ in both liver experiments, probably due to the very low SNR in images produced with $N_G = 8$. On the other hand, using more N_G increases the TE, which as a consequence lowers the SNR. In terms of PNR, using $N_G = 6$ seems to offer the best compromise although it is less

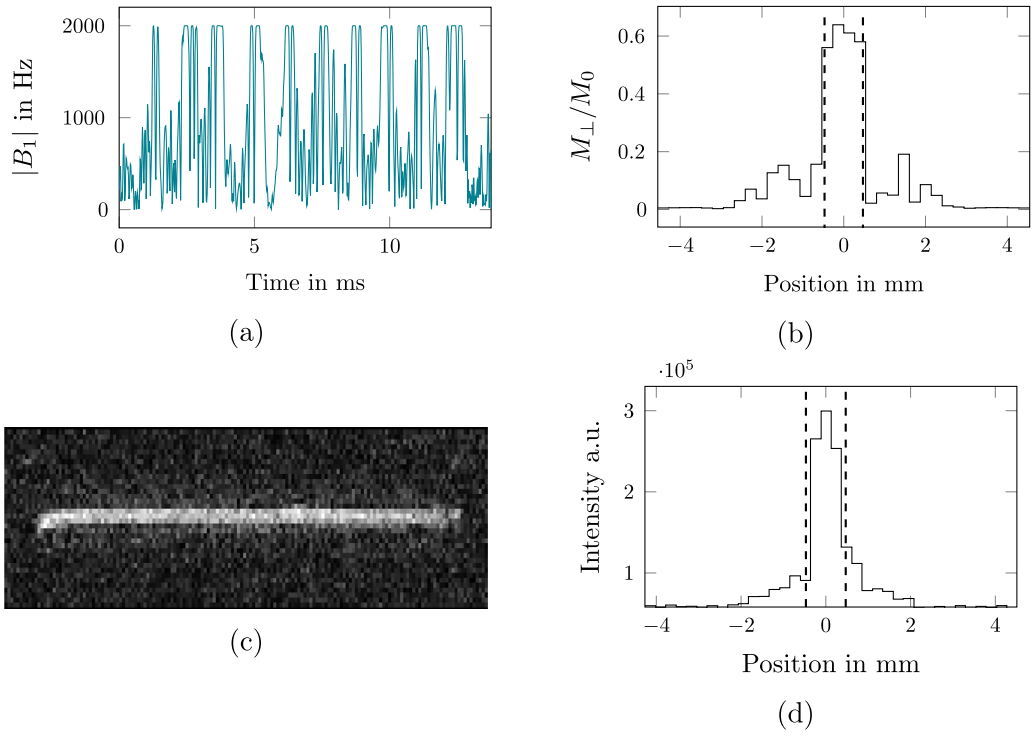

Fig. 7. (a) Magnitude of the optimized RF pulse. (b) Simulated slice profile with the resolution parameters used during the acquisition. (c) Acquired slice profile of the *ex vivo* experiment (liver 1). (d) Row by row signal integration of the acquired slice profile. Dotted lines illustrate the theoretical slice thickness (0.93 mm).

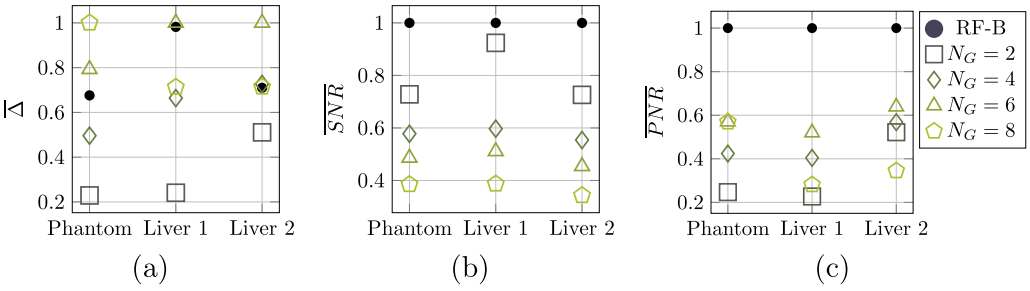

Fig. 8. Comparison between the RF-B scheme and a standard G-B MRE, for different encoding periods numbers (N_G) for both phantom and *ex vivo* experiments (Liver samples). (a) Normalized phase amplitude variation along R_3. Normalized SNR (b) and PNR (c).

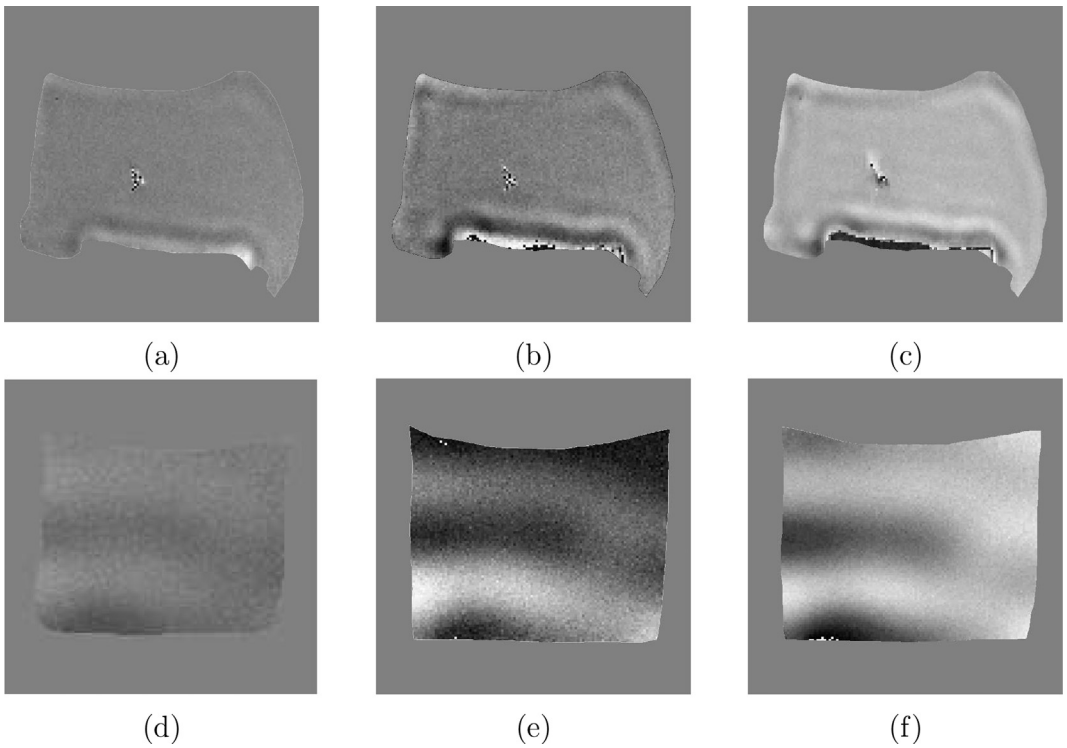

Fig. 9. (a)–(c) Unwrapped masked phase images of the *ex vivo* experiment (liver 1) obtained with (a) the G-B scheme with 2 encoding periods, (b) 6 encoding periods, and (c) the proposed RF-B scheme. (d)–(f) Unwrapped masked phase images of the phantom experiment obtained with (d) the G-B scheme with 2 encoding periods, (e) 6 encoding periods, and (f) the proposed RF-B scheme.

obvious for the phantom study. This is due to the consistently high values of Δ, and reasonable SNR values obtained in all experiments.

For both phantom and *ex vivo* experiments, the proposed RF-B scheme is able to produce relatively high values of Δ while yielding the best SNR. As a result, the PNR is consistently superior to the G-B scheme, regardless of N_G. This is in good agreement with the simulation results of the previous section when low T_2 values were considered. In particular, Fig. 8 shows that similar amplitude variations are obtained with the RF-B scheme and the G-B scheme with $N_G = 6$. However, the SNR results obtained with the RF-B scheme are consistently higher than those obtained with the G-B scheme with $N_G = 6$. As an illustration, the corresponding phase images obtained on the *ex vivo* (liver 1) and on the phantom experiments are shown in Fig. 9. They validate the ability of the proposed scheme to produce images with both high SNR and high phase accumulation.

5. Discussion

This article proposes an innovative method to encode the shear wave propagation into phase images by simultaneously applying a tailored RF pulse and a constant gradient. Unlike standard MRE, no post-excitation oscillating gradients are required, which limits eddy currents and allows extremely short echo times. Having short TE is advantageous in MRE since it minimizes the effect of magnetization coherence loss due to field inhomogeneities, and thus T_2 or $T_2^\star$ decay. This also limits systematic phase errors when gradient-echo sequences are used, avoiding the need for opposite polarity acquisitions. As static field inhomogeneities are considered and compensated during the optimization process, the proposed scheme will produce comparable results for spin-echo and gradient-echo sequences.

The RF based encoding framework induces some practical changes that must be considered during the acquisition. It imposes that the encoded motion is perpendicular to the slice orientation, which limits the flexibility of the current implementation. It also increases the SAR deposition and long TR will have to be considered in order to lower the average power deposition.

Ideally, a new pulse needs to be optimized for every specific application (specific T_2 value, excitation frequency, gradient and motion amplitudes). It is expected that the optimized pulses will not be robust to deviations from the selected excitation frequency. However, variations around the other parameters will likely have a much smaller influence. Taking this into consideration might allow to build a pulse dictionary of reasonable size, from which a dedicated pulse will be selected to perform a specific acquisition.

Future work will focus on releasing the slice orientation constraint, and investigating multi-frequency excitation. The frequency selectivity will also be improved to (i) reduce the number of controlled trajectories, and (ii) limit outer slice interferences that might affect the encoding efficiency. Finally, pre-clinical *in vivo* studies on rat livers will be conducted in order to evaluate the encoding benefit of the RF-B scheme.

6. Conclusion

This study presents a new motion encoding mechanism, based on the simultaneous application of a tailored RF pulse and a constant gradient. The RF pulse is designed with a numerical optimal control algorithm which manipulates the magnetization towards a target state that specifically depends on the phase of the wave propagation. The optimized RF simultaneously performs frequency selective excitation and motion encoding. The encoding mechanism can be intuitively understood and is described analytically. It is based on a $\pi/2$-pulse followed by an even number of π-pulses applied every half-period of the motion. Computing problem-specific RF pulses (considering relaxation times) allows to increase the phase-to-noise ratio on simulation, phantom and

ex vivo experiments when compared to standard MRE sequences. Motion sensitivity seems to be especially improved for low gradient and/or low motion amplitudes, which could prove to be advantageous for limited gradient systems or highly attenuated motion. The proposed approach allows short TE which both limits T_2 signal decay and static phase errors, responsible for undesired phase terms when not refocused (i.e. for gradient-echo sequences). Finally, getting rid of oscillating gradients reduces eddy current artifacts in the acquired image, and allows to relax the constraints on maximum gradient switch rate, which could facilitate the application of high-frequency MRE.

Acknowledgements

This work is supported by the ANR-DFG research program Explosys (Grant No. ANR-14-CE35-0013-01; GL203/9-1) and from the Technische Universität München Institute for Advanced Study, funded by the German Excellence Initiative and the E. U. Seventh Framework Program under Grant No. 291763. This work was performed within the framework of the LABEX PRIMES (ANR-11-LABX-0063/ANR-11-IDEX-0007).

References

[1] R. Muthupillai, D. Lomas, P. Rossman, J. Greenleaf, A. Manduca, R. Ehman, Magnetic resonance elastography by direct visualization of propagating acoustic strain waves, Science 269 (1995) 1854.
[2] S.K. Venkatesh, M. Yin, R.L. Ehman, Magnetic resonance elastography of liver: Technique, analysis, and clinical applications, J. Magn. Reson. Imaging 37 (2013) 544–555.
[3] L.V. Hiscox, C.L. Johnson, E. Barnhill, M.D. McGarry, J. Huston 3rd, E.J. van Beek, J.M. Starr, N. Roberts, Magnetic resonance elastography (mre) of the human brain: technique, findings and clinical applications, Phys. Med. Biol. 61 (2016) R401.
[4] A. Arani, K.L. Glaser, S.P. Arunachalam, P.J. Rossman, D.S. Lake, J.D. Trzasko, A. Manduca, K.P. McGee, R.L. Ehman, P.A. Araoz, In vivo, high-frequency three-dimensional cardiac mr elastography: Feasibility in normal volunteers, Magn. Reson. Med. 77 (2017) 351–360.
[5] J. Rump, D. Klatt, J. Braun, C. Warmuth, I. Sack, Fractional encoding of harmonic motions in mr elastography, Magn. Reson. Med. 57 (2007) 388–395.
[6] C.M. De Bazelaire, G.D. Duhamel, N.M. Rofsky, D.C. Alsop, Mr imaging relaxation times of abdominal and pelvic tissues measured in vivo at 3.0 t: preliminary results, Radiology 230 (2004) 652–659.
[7] B. Leporq, S. Lambert, M. Ronot, V. Vilgrain, B. Van Beers, Simultaneous mr quantification of hepatic fat content, fatty acid composition, transverse relaxation time and magnetic susceptibility for the diagnosis of non-alcoholic steatohepatitis, NMR Biomed. 30 (2017).
[8] P. Garteiser, R.S. Sahebjavaher, L.C. Ter Beek, S. Salcudean, V. Vilgrain, B.E. Van Beers, R. Sinkus, Rapid acquisition of multifrequency, multislice and multidirectional MR elastography data with a fractionally encoded gradient echo sequence, NMR Biomed. 26 (2013) 1326–1335.
[9] S. Conolly, D. Nishimura, A. Macovski, Optimal control solutions to the magnetic resonance selective excitation problem, IEEE Trans. Med. Imag. 5 (1986) 106–115.
[10] T.E. Skinner, T.O. Reiss, B. Luy, N. Khaneja, S.J. Glaser, Application of optimal control theory to the design of broadband excitation pulses for high-resolution NMR, J. Magn. Reson. 163 (2003) 8–15.
[11] H. Liu, G.B. Matson, Radiofrequency pulse designs for three-dimensional MRI providing uniform tipping in inhomogeneous B1 fields, Magn. Reson. Med. 66 (2011) 1254–1266.
[12] M.A. Janich, R.F. Schulte, M. Schwaiger, S.J. Glaser, Robust slice-selective broadband refocusing pulses, J. Magn. Reson. 213 (2011) 126–135.
[13] M.A. Janich, M.A. McLean, R. Noeske, S.J. Glaser, R.F. Schulte, Slice-selective broadband refocusing pulses for the robust generation of crushed spin-echoes, J. Magn. Reson. 223 (2012) 129–137.
[14] K. Kobzar, S. Ehni, T.E. Skinner, S.J. Glaser, B. Luy, Exploring the limits of broadband 90° and 180° universal rotation pulses, J. Magn. Reson. 225 (2012) 142–160.
[15] T.E. Skinner, N.I. Gershenzon, M. Nimbalkar, S.J. Glaser, Optimal control design of band-selective excitation pulses that accommodate relaxation and RF inhomogeneity, J. Magn. Reson. 217 (2012) 53–60.
[16] T.E. Skinner, N.I. Gershenzon, M. Nimbalkar, W. Bermel, B. Luy, S.J. Glaser, New strategies for designing robust universal rotation pulses: application to broadband refocusing at low power, J. Magn. Reson. 216 (2012) 78–87.
[17] M.S. Vinding, I.I. Maximov, Z. Tošner, N.C. Nielsen, Fast numerical design of spatial-selective RF pulses in MRI using Krotov and quasi-Newton based optimal control methods, J. Chem. Phys. 137 (2012).
[18] C.S. Aigner, C. Clason, A. Rund, R. Stollberger, Efficient high-resolution RF pulse design applied to simultaneous multi-slice excitation, J. Magn. Reson. 263 (2016) 33–44.
[19] D. Xu, K.F. King, Y. Zhu, G.C. McKinnon, Z.-P. Liang, Designing multichannel, multidimensional, arbitrary flip angle RF pulses using an optimal control approach, Magn. Reson. Med. 59 (2008) 547–560.
[20] W.A. Grissom, D. Xu, A.B. Kerr, J.A. Fessler, D.C. Noll, Fast large-tip-angle multidimensional and parallel RF pulse design in MRI, IEEE Trans. Med. Imag. 28 (2009) 1548–1559.
[21] A. Massire, M.A. Cloos, A. Vignaud, D.L. Bihan, A. Amadon, N. Boulant, Design of non-selective refocusing pulses with phase-free rotation axis by gradient ascent pulse engineering algorithm in parallel transmission at 7 T, J. Magn. Reson. 230 (2013) 76–83.
[22] A. Sbrizzi, H. Hoogduin, J.V. Hajnal, C.A.T. van den Berg, P.R. Luijten, S.J. Malik, Optimal control design of turbo spin-echo sequences with applications to parallel-transmit systems, Magn. Reson. Med. 77 (2017) 361–373.
[23] M.S. Vinding, B. Guérin, T. Vosegaard, N.C. Nielsen, Local SAR, global SAR, and power-constrained large-flip-angle pulses with optimal control and virtual observation points, Magn. Reson. Med. 77 (2017) 374–384.
[24] B. Bonnard, O. Cots, S. Glaser, M. Lapert, D. Sugny, Y. Zhang, Geometric optimal control of the contrast imaging problem in nuclear magnetic resonance, IEEE Trans. Autom. Control 57 (2012) 1957–1969.
[25] M. Lapert, Y. Zhang, M. Janich, S. Glaser, D. Sugny, Exploring the physical limits of saturation contrast in magnetic resonance imaging, Sci. Rep. 2 (2012).
[26] E. Assémat, M. Lapert, D. Sugny, S.J. Glaser, On the application of geometric optimal control theory to nuclear magnetic resonance, Mathe. Control Related Fields 3 (2013) 375–396.
[27] B. Bonnard, M. Claeys, O. Cots, P. Martinon, Geometric and numerical methods in the contrast imaging problem in nuclear magnetic resonance, Acta Appl. Mathe. 135 (2014) 5–45.
[28] B. Bonnard, O. Cots, Geometric numerical methods and results in the contrast imaging problem in nuclear magnetic resonance, Mathe. Models Methods Appl. Sci. 24 (2014) 187–212.
[29] Y. Chang, D. Wei, S.J. Glaser, X. Yang, Optimized phase-sensitive inversion recovery for MRI contrast manipulation, Appl. Magn. Reson. 46 (2015) 203–217.
[30] E. Van Reeth, H. Ratiney, M. Tesch, D. Grenier, O. Beuf, S.J. Glaser, D. Sugny, Optimal control design of preparation pulses for contrast optimization in MRI, J. Magn. Reson. 279 (2017) 39–50.
[31] E. Van Reeth, H. Ratiney, M. Lapert, S.J. Glaser, D. Sugny, Optimal control theory for applications in magnetic resonance imaging, Pacific J. Mathe. Ind. 9 (2017) 9.
[32] N.I. Gershenzon, T.E. Skinner, B. Brutscher, N. Khaneja, M. Nimbalkar, B. Luy, S. J. Glaser, Linear phase slope in pulse design: Application to coherence transfer, J. Magn. Reson. 192 (2008) 235–243.
[33] K. Kobzar, B. Luy, N. Khaneja, S.J. Glaser, Pattern pulses: design of arbitrary excitation profiles as a function of pulse amplitude and offset, J. Magn. Reson. 173 (2005) 229–235.
[34] J. Assländer, S.J. Glaser, J. Hennig, Spin echoes in the regime of weak dephasing, Magn. Reson. Med. 75 (2016) 150–160.
[35] P.M. Lefebvre, E. Van Reeth, H. Ratiney, O. Beuf, E. Brusseau, S.A. Lambert, S.J. Glaser, D. Sugny, D. Grenier, K. Tse Ve Koon, Active control of the spatial MRI phase distribution with optimal control theory, J. Magn. Reson. 281 (2017) 82–93.
[36] L.S. Pontryagin, Mathematical Theory of Optimal Processes, CRC Press, 1987.
[37] N. Khaneja, T. Reiss, C. Kehlet, T. Schulte-Herbrüggen, S.J. Glaser, Optimal control of coupled spin dynamics: design of NMR pulse sequences by gradient ascent algorithms, J. Magn. Reson. 172 (2005) 296–305.
[38] P. de Fouquieres, S. Schirmer, S. Glaser, I. Kuprov, Second order gradient ascent pulse engineering, J. Magn. Reson. 212 (2011) 412–417.
[39] P. Lefebvre, K. Tse Ve Koon, E. Brusseau, S. Nicolle, J.-F. Pallierne, S. Lambert, D. Grenier, Comparison of viscoelastic property characterization of plastisol phantoms with magnetic resonance elastography and high-frequency rheometry, in: 38th IEEE Annual International Conference of the Engineering in Medicine and Biology Society (EMBC) 2016, Orlando, United States, 2016.